In-Orbit Calibration of FengYun-3C Microwave Radiation Imager: Characterization of Backlobe Intrusion for the Hot-Load Reflector

Xinxin Xie, Wanting Meng, Kesong Dong, Songyan Gu, and Xue Li

***Abstract*—This study presents a correction algorithm to remove the backlobe intrusion from the hot-load reflector of microwave radiation imager (MWRI) on-board China FengYun-3C (FY-3C) meteorological satellite. Discontinuities in the radiometric gain of MWRI, due to inaccurate backlobe spillover of the hot-load reflector, have been diagnosed. A physical correction method, relating the radiometric gain difference between two distinct backlobe scenes to the spillover of the hot-load reflector, is thus established to estimate the in-orbit spillover factor of the MWRI hot-load reflector. Meanwhile, it is found that brightness temperature (TB) at each 1° × 1° grid could not address the backlobe pattern appropriately, leading to abrupt changes in the radiometric gain occurring near the coastlines. To better represent the backlobe spillover, the effective backlobe TB is now averaged over a 4° × 4° area from advanced microwave scanning radiometer-observed TBs, which is now in a finer resolution of 0.25° × 0.25°. With the adjusted spillover for the hot-load reflector, anomalous behaviors of the radiometric gain are mitigated effectively and the improvement at the coastlines is pronounced, inducing TB variation up to 2 K in magnitude at the 10.65 GHz channel. Although the algorithm presented in this study is only restricted to channel frequencies up to 23.8 GHz due to its accuracy limitation, it could tackle similar issues for those microwave radiometers not capable of in-orbit backlobe maneuvers and receiving the radiances inevitably from the outer edge of the hot-load or cold-sky reflectors.**

***Index Terms*—Backlobe spillover, calibration, FengYun-3C (FY-3C), microwave radiation imager (MWRI), microwave radiometer.**

I. Introduction

MICROWAVE radiation imager (MWRI) is a conically scanning microwave radiometer on-board China polar-orbiting FengYun-3C (FY-3C) satellite [1]. Operating at 10.65, 18.7, 23.8, 36.5, and 89 GHz with dual polarization, MWRI has served as an important instrument to meteorological research on Earth surveillance and severe weather monitoring [2], [3].

FY-3C MWRI is a total power radiometer and was designed to deploy a hot-load parabolic reflector and a cold-sky mirror to reflect the radiance from the hot load and the cosmic background into the primary reflector, respectively, as "the hot and cold points" at each scan in the conventional two-point calibration approach [4]–[7]. The hot-load reflector of MWRI makes the calibration configuration unique and further becomes one of the constraints in the calibration accuracy. The detailed comparisons of MWRI-observed brightness temperature (TB) with radiative transfer (RT) modeled background results suggested that an underestimation of the emission from the hot-load reflector causes calibration bias discrepancies between the ascending and descending phases of the orbits [7]–[9]. In addition, when viewing the calibration hot point, radiance originating from the Earth can enter the feedhorn assembly from the outer edge of the hot-load reflector (hereinafter backlobe spillover). Inevitably, the backlobe intrusion of the hot-load reflector contaminates the calibration hot point and could result in uncertainties in the calibration process when it is not removed properly.

The accurate knowledge of the backlobe spillover is still very difficult to acquire from prelaunch antenna measurements in anechoic chambers. An error of 1% in the backlobe spillover factor corresponds to 2 K calibration bias for an Earth scene of 200 K [10], [11]. In-orbit backlobe maneuvers have been conducted to space-borne instruments, e.g., tropical rainfall measuring mission microwave imager (TMI), global precipitation measurement microwave imager (GMI), and WindSat, in order to refine the estimates of the spillover of the primary reflector or the cold-sky reflector, when the reflector backlobe was fully subtended by the Earth over ocean [11]–[15]. For some spacecrafts unable to accomplish in-orbit maneuvers, derivation of the in-orbit backlobe spillover was usually achieved via an overall agreement between the in-orbit observations and the RT-calculated background TBs [10]. Smoothing the radiometric gain along the orbit was also performed to eliminate the contamination at the hot point for in-orbit microwave radiometers in previous research [16], [17].

Uncertainties in the RT calculations could further introduce calibration biases in the adjustment process. Instead of using

Manuscript received December 8, 2020; revised March 21, 2021; accepted April 21, 2021. Date of publication April 27, 2021; date of current version July 14, 2021. This work was supported in part by the National Key Research and Development Program of China under Grant 2018YFB0504900 and Grant 2018YFB0504902, in part by the National Natural Science Foundation of China under Grant 41805024 and Grant 42005105, and in part by the Joint Open Research Fund Program of State Key Laboratory of Hydroscience and Engineering and Tsinghua–Ningxia Yinchuan Joint Institute of Internet of Waters on Digital Water Governance under Grant sklhse-2021-Iow08. *(Corresponding author: Xinxin Xie.)*

Xinxin Xie is with the School of Atmospheric Sciences of Sun Yat-Sen University, the Key Laboratory of Tropical Atmosphere-Ocean System of Ministry of Education, Zhuhai 519082, China, and also with the Southern Marine Science and Engineering Guangdong Laboratory, Zhuhai 519082, China (e-mail: xiexx25@mail.sysu.edu.cn).

Wanting Meng, Kesong Dong, and Xue Li are with the Shanghai Spaceflight Institute of TT&C and Telecommunication, Shanghai 201109, China (e-mail: wanting_meng@163.com; dslexwpg@163.com; 39740693@qq.com).

Songyan Gu is with the National Satellite Meteorology Center, Beijing 100081, China (e-mail: gusy@cma.gov.cn).

Digital Object Identifier 10.1109/JSTARS.2021.3075969

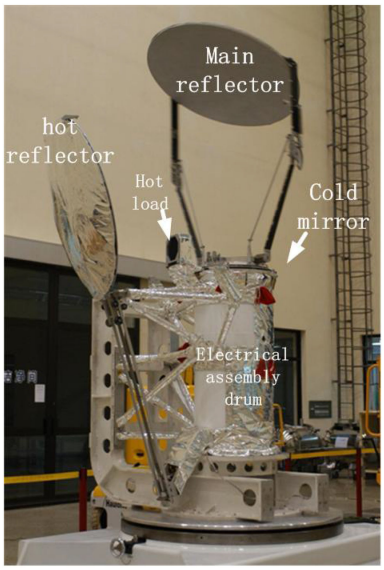

Fig. 1. FY-3C MWRI with its hot reflector, main reflector, and hot load. The cold mirror was mounted on the top of the satellite with the arrow indicating its location here (the mirror was missing in this photo) [7].

RT results as a reference standard, we propose, in this study, a physical correction algorithm to calculate the in-orbit backlobe spillover of the MWRI hot-load reflector. To ensure accurate estimates of the backlobe intrusion, we establish the relation between the spillover factor of the hot-load reflector and the radiometric gain when the satellite is flying across the coastlines. This method is independent of the RT reference standard and enables in-orbit adjustment of reflector spillover for those microwave imagers, which also suffer from the severe backlobe spillover of the hot-load reflector or cold-sky reflector from the Earth.

The rest of this article is structured as follows. With an inspection into the anomalous radiometric gain, Section II identifies MWRI calibration issues caused by backlobe contamination entering the calibration hot view from the MWRI hot-load reflector. In Section III, the correction algorithm, which relates the backlobe intrusion of the hot-load reflector to the abrupt changes in the radiometric gain at the coastlines, is developed. In Section IV, the improvement of the radiometric gain due to the refined backlobe spillover of the hot-load reflector is discussed with corrected TBs in the latitudinal direction. Finally, Section V concludes the article.

II. Radiometric Gain Anomalies and Diagnosis

At each scan, MWRI is calibrated by viewing the hot load and the cosmic background alternately. The configuration of MWRI is shown in Fig. 1. More details about the MWRI calibration algorithm can be found in [6] and [7]. The radiometric gain G of MWRI is defined as

$$G = \frac{\mathrm{TB}_H - \mathrm{TB}_C}{V_H - V_C} \tag{1}$$

where TB is the brightness temperature, V is the MWRI-observed voltage, and the subscripts H and C represent the hot and cold views in the calibration, respectively.

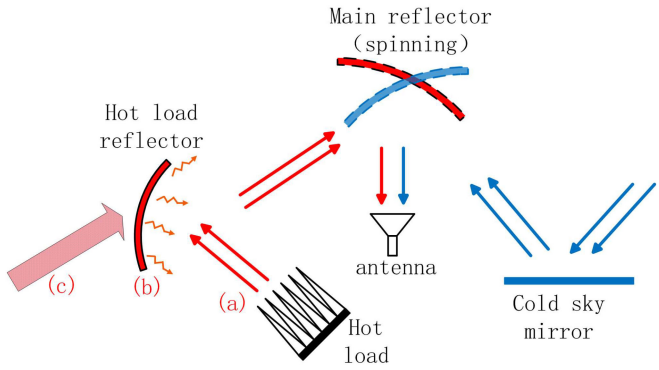

Fig. 2. Schematic diagram of the MWRI calibration system. The hot view TB is contributed by (a) hot-load emission, (b) emissive hot-load reflector, and (c) backlobe intrusion from the Earth scenes.

According to the propagation path of microwave radiances in the MWRI calibration system, the hot view TB_H is composed of three parts, i.e., emission from the hot load, emission of the hot-load reflector, and backlobe intrusion of the hot-load reflector [6], [7] (see Fig. 2)

$$\begin{aligned}\mathrm{TB}_H &= \eta_T(1-\varepsilon_H)T_H + \varepsilon_H\eta_T T_{\mathrm{hot}} + (1-\eta_T)T_{ET} \\ &= \eta_T[(1-\varepsilon_H)T_H + \varepsilon_H T_{\mathrm{hot}}] + (1-\eta_T)T_{ET} \\ &= \underline{\eta_T T_{BB}} + \underline{\underline{(1-\eta_T)T_{ET}}} \\ &= \underbrace{\begin{matrix}\text{emission from} \\ \text{the hot - load reflector} \\ \text{and the hot load}\end{matrix}} + \underline{\underline{\begin{matrix}\text{backlobe radiation of} \\ \text{the hot - load reflector}\end{matrix}}}\end{aligned} \tag{2}$$

where ε_H is the emissivity of the hot-load reflector, T_H is the effective TB of the hot load, which is reflected by the hot-load reflector into the main reflector, T_{hot} is the temperature of the hot-load reflector, $(1-\eta_T)$ is the backlobe spillover factor of the hot-load reflector, T_{ET} is from the backlobe of the hot reflector, and T_{BB} is the sum of the emission from the hot-load reflector and the hot load. When extending the hot-load emission reflected off the hot-load reflector into the primary reflector, the center of the extension is intercepted by the Earth at a specific pixel. Currently, TB at each $1^\circ \times 1^\circ$ grid point is used as the backlobe radiances [T_{ET} in (2)], which is determined by the monthly mean advanced microwave scanning radiometer (AMSR-2) observations with a spatial resolution of $1^\circ \times 1^\circ$.

The cold mirror was deployed at the top of the satellite with its back directly attached to the satellite platform (see Fig. 1). The backlobe spillover of the cold-sky mirror was not detected during the observations. Therefore, the cold view TB_C received from the calibration cold view is the sum of the cold mirror emission and reflection (see Fig. 2). By defining ε_C the cold mirror emissivity, T_{CS} the cosmic background, and T_{CM} the measured temperature of the cold mirror, TB_C is expressed as

$$\begin{aligned}\mathrm{TB}_C &= \underline{(1-\varepsilon_C)T_{CS}} + \underline{\underline{\varepsilon_C T_{CM}}} \\ &= \underbrace{\begin{matrix}\text{cold - sky} \\ \text{radiation}\end{matrix}} + \underline{\underline{\begin{matrix}\text{emission of} \\ \text{the cold - sky mirror}\end{matrix}}}.\end{aligned} \tag{3}$$

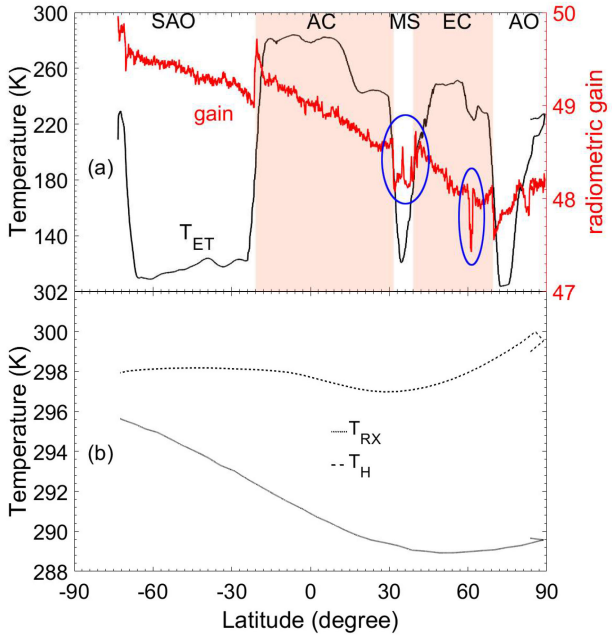

Fig. 3. From top to bottom. (a) Radiometric gain (red solid line) and the backlobe TB (T_{ET}, black solid line) are shown as a function of latitude at the 10.65 H channel. The continents are highlighted by the red shaded areas and AO, EC, MS, AC, and SAO are the Arctic Ocean, European Continent, Mediterranean Sea, African Continent, and South Atlantic Ocean, respectively. (b) Receiver temperature (T_{RX}, black dotted line) and hot-load temperature (T_H, black dashed line) are shown as a function of latitude at the 10.65 H channel. The spikes encircled by blue ellipses in the regions of EC and MS correspond to the Baltic Sea and Asia Minor Peninsula, respectively.

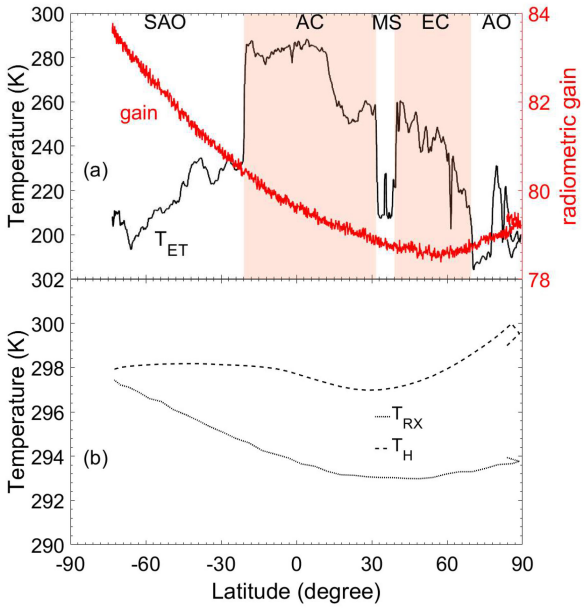

Fig. 4. Same as Fig. 3 except for the 89 H channel.

Inserting (2) and (3) in (1), the radiometric gain of MWRI is, thus, rewritten as follows:

$$G = \frac{\eta_T T_{BB} + (1-\eta_T)T_{ET} - \mathrm{TB}_C}{V_H - V_C}. \tag{4}$$

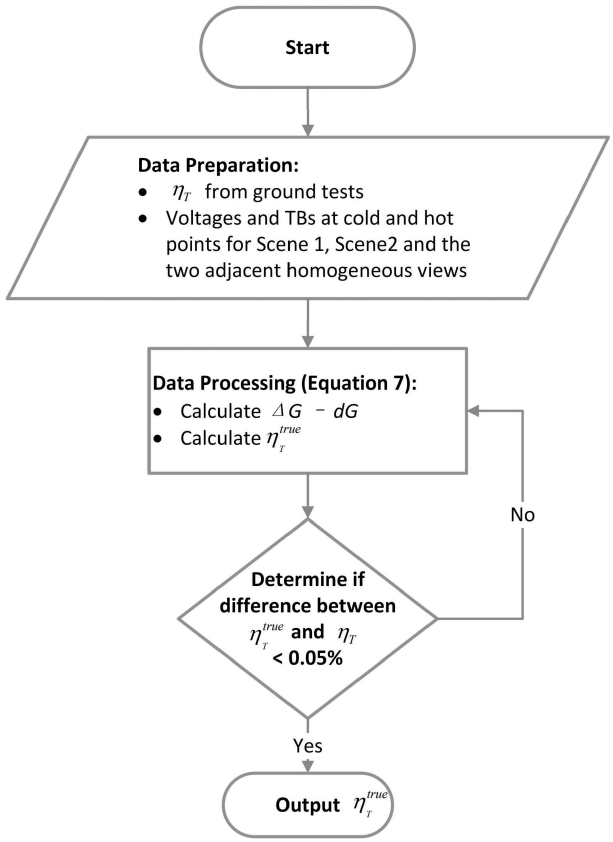

Fig. 5. Flowchart of the algorithm.

We show, in Fig. 3 (see Fig. 4) at the 10.65 H (89 H) channel, the radiometric gain, the temperatures of the hot load and receiver, and the backlobe TB as a function of latitude in one descending orbit on January 1st, 2019. In this track, the spacecraft flies over the Arctic Ocean, European Continent (EC), Mediterranean Sea (MS), African Continent (AC), and South Atlantic Ocean (SAO) in sequence. Anomalous behaviors of the radiometric gain at the 10.65 H channel are identified with abrupt changes near the coastlines, wherever the corresponding backlobe TB increases or decreases dramatically by ∼150 K [see Fig. 3(a)]. The spikes of the radiometric gain in the regions of EC and MS correspond to the Baltic Sea and Asia Minor Peninsula, respectively. The hot-load temperature and the receiver temperature are also examined for the same orbit. The variation of the hot-load temperature is within 3.1 K in this orbit, while the receiver temperature first decreases from 289.7 to 288.9 K and then increases gradually to 295.6 K, when FY-3C flies southward [see Fig. 3(b)].

Different from the 10.65 H channel, the radiometric gain at the 89 H channel has no such abrupt changes for the same descending pass, although the backlobe of the hot-load reflector still views an 80 K TB difference between the land and ocean scenes [see Fig. 4(a)]. The receiver temperature at the 89 H channel varies in 4.6 K for this orbit [see Fig. 4(b)].

Theoretically, the radiometric gain is strongly correlated to the receiver temperature that exhibits periodic in-orbit variation [17], [18]. The short-term gain variation for MWRI, however,

is not correlated with the change of the receiver temperature or the hot-load temperature but strongly correlated to the backlobe scene, leading to such discontinuities, as shown in Fig. 3. When examining (4), the cold-sky mirror does not receive the Earth radiation. It is, thus, speculated that the hot view is contaminated by the Earth scene from the outer edge of the hot-load reflector and the backlobe intrusion has not been completely removed by the calibration process, resulting in gain anomalies correlating to the backlobe scene at the 10.65 H channel (see Fig. 3). Presumably, the fraction of the antenna pattern that intercepts the Earth (η_T) may be either overestimated or underestimated in the calibration process since it is still one of the major challenges to specify in the prelaunch phase. An underestimated (overestimated) spillover generally enhances (reduces) the TB component originating from the hot-load emission and further augments the discontinuous gain "step" between the continent and ocean (see Fig. 3). While for the 89 H channel, the backlobe spillover is usually very small, as predicted by the on-ground antenna analysis (0.2%), and the radiometric gain only exhibits its strong correlation to the receiver temperature instead of the backlobe scenes (see Fig. 4).

The backlobe pattern of the hot-load reflector derived from the electromagnetic model analysis also poses some uncertainties. As shown in Fig. 3, using the TB at each $1^\circ \times 1^\circ$ pixel as the backlobe radiation in the current in-orbit calibration process is definitely not a good approximation for the backlobe scene. When the MWRI backlobe geolocation transits from the continent to the ocean (e.g., at a latitude of $\sim$20 °S), a small spike toward a larger gain value appears in a few scans near the coastlines, indicating inaccurate characterization of the backlobe TB in the calibration process [see Fig. 3(a)]. As the spacecraft is flying across the coastline southward, from the AC to SAO, the cooler ocean, which is beginning to enter the backlobe view, is still not taken into account in the backlobe radiation. Thus, the backlobe TB is overestimated and causes an abrupt augmentation in the gain value near the coastlines, i.e., the spike near the latitude of $\sim$20°S. With the flight further to the South, the warmer land is still not yet completely moving out of the backlobe view but not considered as a part of the backlobe intrusion anymore, inducing an underestimation in the backlobe radiation and a relatively lower gain following the spike in the previous scans.

Discontinuities in the gain have been observed for MWRI and its anomalous behaviors due to the backlobe intrusion of the hot-load reflector could further deteriorate the calibration accuracy. Correction is, thus, necessary for the in-orbit refinement of the backlobe spillover of the MWRI hot-load reflector.

III. Correction Algorithm

In this study, we use the radiometric gain double-difference method to correct the in-orbit backlobe spillover of the hot-load reflector. The radiometric gain single difference for the double-difference method is the difference of the radiometric gain between two backlobe scenes in one orbit. One of the single differences is defined as dG the "true" radiometric gain single difference between Scene 1 and Scene 2, assuming the backlobe intrusion is completely removed in the calibration process with the accurate backlobe spillover factor ($1-\eta_T^{\text{true}}$). Another single difference, i.e., the unadjusted single difference ΔG, is derived with the inaccurate backlobe spillover ($1-\eta_T$).

Given (4), the "true" radiometric gain single difference is expressed as

$$\begin{aligned} dG &= G_1^{\text{true}} - G_2^{\text{true}} \\ &= \eta_T^{\text{true}} \left(\frac{T_{BB}^1 - T_{ET}^1}{V_H^1 - V_C^1} - \frac{T_{BB}^2 - T_{ET}^2}{V_H^2 - V_C^2} \right) + \frac{T_{ET}^1 - \text{TB}_c^1}{V_H^1 - V_C^1} - \frac{T_{ET}^2 - \text{TB}_c^2}{V_H^2 - V_C^2} \end{aligned} \tag{5}$$

where subscripts 1 and 2 represent the two distinct backlobe views from Scene 1 and Scene 2, respectively.

When the backlobe spillover factor ($1-\eta_T$) is not adjusted accurately, the unadjusted radiometric gain single difference between Scene 1 and Scene 2, i.e., ΔG , can be also derived by (4) and (5).

With the two single differences ΔG and dG, the radiometric gain double difference between Scene 1 and Scene 2 can be derived as

$$\begin{aligned} \Delta G - dG &= G_1 - G_2 - (G_1^{\text{true}} - G_2^{\text{true}}) \\ &= (\eta_T - \eta_T^{\text{true}}) \left(\frac{T_{BB}^1 - T_{ET}^1}{V_H^1 - V_C^1} - \frac{T_{BB}^2 - T_{ET}^2}{V_H^2 - V_C^2} \right). \end{aligned} \tag{6}$$

We then obtain the true backlobe spillover of the hot-load reflector via the relationship between the radiometric gain double difference and the backlobe TBs at Scene 1 and Scene 2, accordingly

$$\eta_T^{\text{true}} = \eta_T - \frac{\Delta G - dG}{\frac{T_{BB}^1 - T_{ET}^1}{V_H^1 - V_C^1} - \frac{T_{BB}^2 - T_{ET}^2}{V_H^2 - V_C^2}}. \tag{7}$$

The backlobe spillover only correlates to the observations from Scene 1 and Scene 2 and is independent of other calibration parameters (7). To solve the "true" backlobe spillover factor, two scenes should be defined to calculate the two single gain differences for (7), as well as the measured TBs and the voltages at the cold and hot views.

To avoid uncertainties resulted from the varying environments, the time duration between Scene 1 and Scene 2 should be reduced. The impacts of the in-orbit environment are, thus, mitigated and only limited variation occurs for the cold-sky voltages and the hot-load temperatures in Scene 1 and Scene 2**.** Therefore, the scan line number between Scene 1 and Scene 2 is selected to be within 100, which equals the scan duration no longer than 180 s. Thus, the variation of the effective hot-load TB is on the order of a small fraction of a Kelvin, i.e., less than 0.2 K, and the observed hot and cold voltages also have negligible change. Another criterion to select the backlobe Scene 1 and Scene 2 is that the backlobe of the hot-load reflector is fully subtended by the warm land and cold ocean, respectively, to eliminate possible uncertainties brought by inhomogeneous backlobe views and to provide two distinct scenes (Scene 1 and Scene 2). We, therefore, select Scene 1 and Scene 2 as the scans before and after the spacecraft crossing the coastlines, respectively, where a maximum TB difference between the two scenes could be expected in a short time period.

To specify the true gain difference dG, we approximate dG from homogeneous or near homogeneous adjacent backlobe

views (either continent or ocean). The scan duration (scan line number) between the two adjacent scenes is the same as that of between Scene 1 and Scene 2, as the radiometric gain is expected to vary continuously and monotonously in a short time period.

Iteration is applied to solve (7). The threshold of the backlobe spillover $(1-\eta_T)$ is set to be 0.1, i.e., $\eta_T = 0.9$, and the radiometric gain double difference is calculated with the backlobe spillover factor from the on-ground analysis for the first iteration step. In each iteration step, substituting η_T with η_T^{true} from the last iteration to calculate the radiometric gain double difference, a new η_T^{true} is, thus, derived in (7). Iteration stops only when the difference between η_T^{true} and η_T is less than 0.05%, allowing only 0.1 K bias at the backlobe view of 200 K. A diagram to show how the algorithm works is provided in detail in Fig. 5.

The accuracy of this correction algorithm highly depends on the contrasting TB between Scene 1 and Scene 2. At each channel, the observed voltage difference between the hot and cold views is on the order of 5 V and the observed TB discrepancy between Scene 1 and Scene 2 mainly determines when the iteration could stop. With a TB difference of 150 K, the accuracy of the algorithm may reach up to 0.03% if the gain double difference is 0.01; while it is only on the order of 0.1% at a 50 K TB difference between Scene 1 and Scene 2. Note that the uncertainties in the backlobe TB difference between Scene 1 and Scene 2, at least at an order of magnitude less than the backlobe TB, can hardly affect the accuracy of the backlobe spillover in the algorithm.

The characterization of the backlobe intrusion now reduces to specifying the backlobe TB values at each scan. Since the launch of FY-3C, AMSR-2 monthly TB at each $1^\circ \times 1^\circ$ pixel has been taken as the backlobe radiation of MWRI hot-load reflector in the calibration process. To ensure a relatively accurate spillover region, we now adjust the AMSR-2 monthly observations in a finer resolution of $0.25^\circ \times 0.25^\circ$ and the TBs over a larger area is taken as the representative backlobe region. An effective area of $4^\circ \times 4^\circ$ is selected and the averaged TBs in the $4^\circ \times 4^\circ$ box represent the background radiation, when the spikes of the gain occurring at coastlines are minimized. Note that the derivation of the backlobe spillover with the radiometric gain double-difference method is not sensitive to the backlobe TB values at Scene 1 and Scene 2, which are supposed to be homogeneous ocean and land areas.

The algorithm presented in this study restricts to horizontally and vertically polarized channels at the frequencies of 10.65, 18.7, and 23.8 GHz, which are seriously affected by the backlobe intrusion with severe discontinuities in the radiometric gain. First, as discussed above, the method requires distinct backlobe TBs for Scene 1 and Scene 2 and the ambiguous coastlines at 36.5 and 89 GHz are not applicable in this condition. Another reason is that for higher frequency channels above 36.5 GHz, spillover factors of the hot-load reflector are usually small (0.2% from the prelaunch analysis).

IV. Results and Discussion

We have chosen MWRI one-month observation dataset in January 2019 in order to derive the spillover of the hot-load reflector and considered only the descending orbits across the African continent into the relatively homogeneous South Atlantic Ocean to meet the criteria for the correction algorithm, as described in Section III.

TABLE I
Backlobe Spillover Factor $(1-\eta)$ of the MWRI Hot-Load Reflector Before and After Correction at the 10.65V/H, 18.7V/H, and 23.8V/H Channels

Channel No.	Frequency (GHz)	(1-η) Before correction	(1-η) After correction (std)
1	10.65V	2.69%	3.48% (0.0041)
2	10.65H	3.12%	3.07% (0.0027)
3	18.7V	1.88%	3.03% (0.0089)
4	18.7H	2.52%	3.24% (0.0045)
5	23.8V	1.10%	0.91% (0.0044)
6	23.8H	1.45%	0.83% (0.0036)

The backlobe spillover factor of the MWRI hot-load reflector decreases with increasing channel frequency, from ∼3% at 10.65 GHz channels to less than 1% at 23.8 GHz channels (see Table I). Comparing to the in-orbit analysis, the backlobe spillover was generally underestimated at launch and ∼1% difference between spillover factors before and after correction is found for the 10.65 and 18.7 channels, as given in Table I. The standard deviation of the spillover factor ranges from 0.0027 to 0.0089 while lying in the interval between 0.003 and 0.004 for most channels. As discussed in Section III, the accuracy of the algorithm highly depends on to what extent microwave radiance over land is distinguished from coastal waters at the channels. The standard deviation of spillover is only 0.0027 at the 10.65 H channel since TBs over land could be 150 K warmer in contrast to the cold ocean; while it is up to 0.0089 with much more blurring coastlines at the 18.7V channel.

For the same descending orbit, as illustrated in Figs. 3 and 4, the MWRI radiometric gain is shown before and after spillover correction at the 10.65V/H, 18.7V/H, and 23.8V/H channels in Fig. 6. The improvement in the discontinuities of the radiometric gain is clearly visible, especially for the 10.65V and 10.65 H channels where relatively greater spillover factors are expected than other channels. The radiometric gain "step" between the land and ocean is diminished and the spikes near the coastlines are also removed effectively after the spillover correction is applied in the calibration process.

We checked carefully the radiometric gain at the 10.65 H channel, as the corrected spillover factor at this channel leads to pronounced improvements in the continuities of the radiometric gain. At the latitude between 30 °N and 90 °N, the radiometric gain is generally reduced after correction while it has negligible changes from 30 °N southward (see Fig. 6). As the spacecraft continues flying southward, the value is enhanced by ∼0.2 in magnitude over the South Atlantic Ocean until the following ascending pass. The cause for this is that, with an increasing receiver temperature from 30 °N southward, an overestimated spillover significantly reduces the contribution from the hot load to the gain, leading to a lower radiometric gain over the cold ocean. Near the equatorial region, the effective hot-load

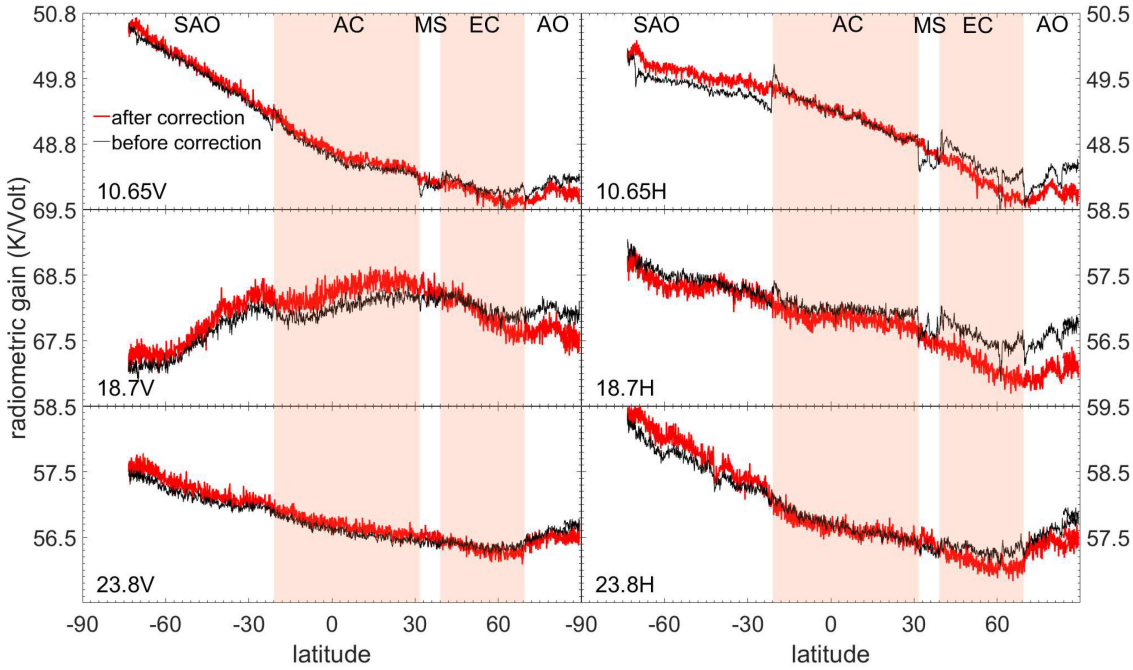

Fig. 6. MWRI radiometric gain before and after backlobe spillover correction is shown as a function of latitude for the 10.65, 18.7, and 23.8 GHz channels in the same descending orbit of Fig. 3. The continents are highlighted by the red shaded areas and AO, EC, MS, AC, and SAO are the Arctic Ocean, European Continent, Mediterranean Sea, African Continent, and South Atlantic Ocean, respectively.

temperature is comparable with the backlobe TB and the radiometric gain is, thus, not sensitive to the spillover change. Note that the residual uncertainties in the radiometric gain could still exist in the calibration process. In some observation scenarios, e.g., extreme weather events, backlobe TBs mapped from the one-month mean AMSR-2 observations could be up to tens of Kelvins away from the truth and further introduce calibration biases on the order of 1–2 K. Moreover, additional uncertainties arising from solar intrusion can cause some spikes in the gain at all channels when the sensor is exposed to the sunlight.

TB correction due to the spillover adjustment is shown in Fig. 7 along the same descending orbit. TB changes by about 2 K in magnitude at all channels, from −1 K in the Northern hemisphere to 1 K in the Southern hemisphere. Homogeneous backlobe scenes over ocean and continent provide a good opportunity to examine TB damping or enhancing due to the spillover correction. At the latitude between 30 °N and 20°S, where the backlobe intercepts only the African continent, TB is slightly enhanced and a magnitude up to 1.7 K is only found for the 18.7V channel. When the backlobe of the hot-load reflector is completely subtended by the cold ocean (latitude from 20 °S to 60 °S), TB increases discernibly by ∼0.4 K at the 10.65 H channels in consistent with the corrected radiometric gain, as shown in Fig. 6. It is noticed that the refinement of both the spillover factor and the backlobe view contributes to a maximum TB variation occurring at the coastlines, where the characteristic of the radiometric gain has been improved remarkably. Due to the broader backlobe pattern for the 10 GHz channels, TB variation at the coastlines is on the order of 2 K, while for the 23.8 GHz channels, TB change is limited within 1 K.

Zonal mean TB difference before and after correction is shown for each channel with a latitude grid of 1° with the one-month observations (see Fig. 8). Cloud and precipitation scenarios were screened over the ocean following the work done by Kroodsma *et al.* [19] and Colton and Poe [20]. Complying with the TB difference as a function of latitude, as shown in Fig. 7, the increase of the zonal mean TB difference toward the southern hemisphere is on the order of 1.5 K at each channel. In the northern hemisphere, a noticeable decrease in TB at all channels is found after the spillover correction, while TB slightly increases in the southern hemisphere, except for the 18.7H channel where TB is damped both in the northern and southern hemispheres.

It is not easy, however, to verify the spillover correction with direct comparisons to RT simulations over the ocean, when the TB improvement after backlobe correction is on the order of the RT accuracy. Using the modeled TBs as a reference, thus, requires further assessment of the RT results. Despite the most pronounced response along the coastlines, uncertainties in the surface emissivity of geographically complex coastlines and continental areas, which are still not yet fully understood, could be carried into RT calculations and makes the validation with simulations much more complicated.

V. Conclusion

This study has described the correction algorithm to correct the backlobe intrusion of the hot-load reflector for MWRI onboard FY-3C. Not only the backlobe spillover factor but also the backlobe TBs were adjusted at each channel with one-month observations in January 2019.

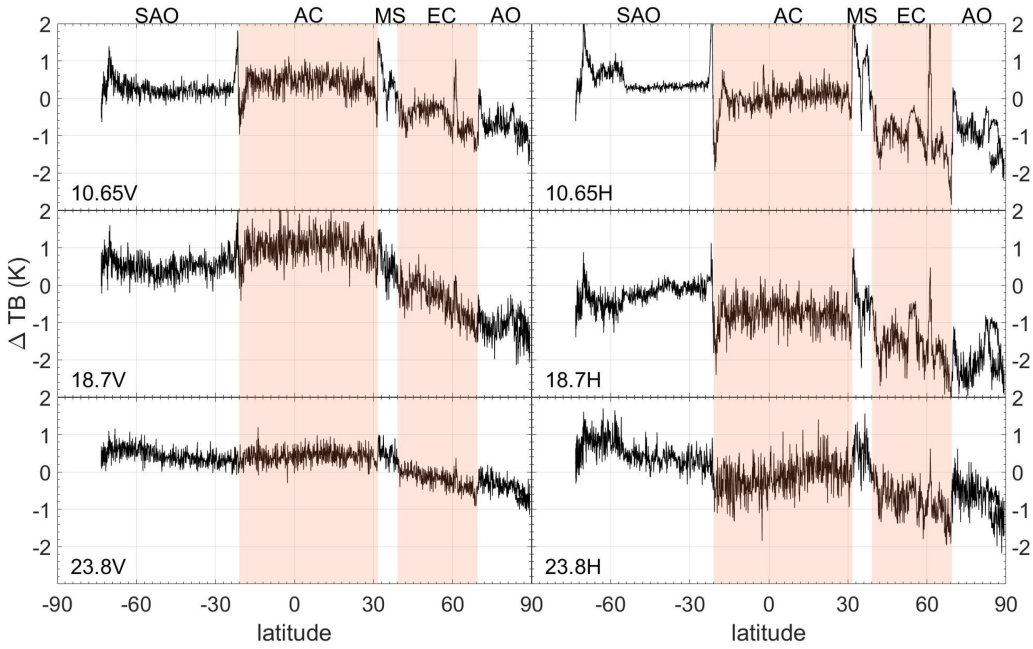

Fig. 7. TB difference before and after spillover correction is shown as a function of latitude for the 10.65V/H, 18.7V/H, and 23.8V/H GHz channels in the same descending orbit of Fig. 2. The continents are highlighted by the red shaded areas and AO, EC, MS, AC, and SAO are the Arctic Ocean, European Continent, Mediterranean Sea, African Continent, and South Atlantic Ocean, respectively. The spikes in the MS and EC region correspond to the Minor Asia Peninsula and Baltic Sea.

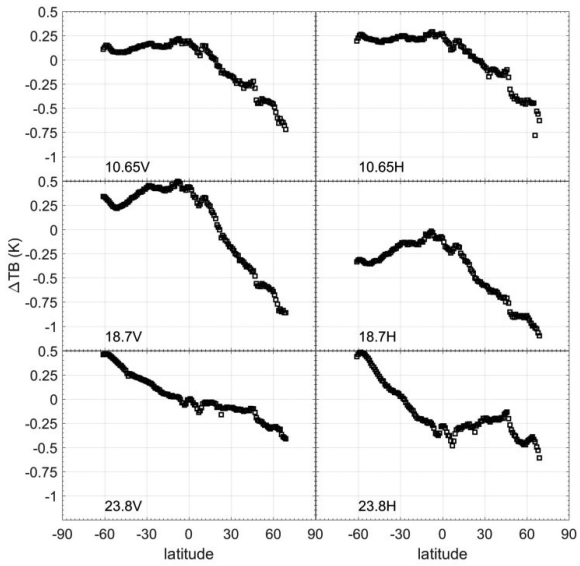

Fig. 8. Zonal mean TB correction after spillover correction as a function of latitude over the calm and clear ocean for the 10.65V/H, 18.7V/H, and 23.8V/H GHz channels in January 2019.

MWRI radiometric gain, which is theoretically correlated to the receiver temperature, was found to be strongly correlated to the backlobe view with anomalous discontinuities along the orbits. By relating the radiometric gain double difference to two distinct backlobe views, the backlobe spillover factor of the hot-load reflector was adjusted when the satellite crosses the African continent to marine regions. The backlobe radiation was considered as an effective TB averaged over an area of 4° $\times$ 4° to achieve a better estimation of the backlobe region and to eliminate the abrupt changes in the radiometric gain.

The spillover of the hot-load reflector was found to be over/underestimated at launch. Attributed to accurate estimation of the backlobe intrusion, calibration anomalies of the radiometric gain were mitigated effectively. It has been shown that the algorithm is effective in removing the discontinuities and spikes in the radiometric gain. After applying the correction algorithm in the calibration process, the observed TB at the land and ocean boundaries has been significantly improved on the order of 1–3 K, depending on the channels. Along the latitudinal direction, TB correction over the ocean was up to 1 K in magnitude.

The same method will be promoted to the MWRIs on-board FY-3B and FY-3D to adjust the in-orbit backlobe spillover since the design of these instruments is identical. The algorithm could also be applied to the microwave radiometers suffering from the severe backlobe spillover, when it is still a challenge to estimate those calibration parameters accurately in the prelaunch phase. However, it is not sensitive enough to the channels with frequencies above 36.5 GHz, where it is difficult to detect the obscured coastlines and the parabolic reflector has a much smaller backlobe spillover factor. To further refine the in-orbit adjustments of MWRI calibration, backlobe maneuvers, which can provide the cosmic background as a stable cold reference, become necessary and have been proposed to the next generation of FY satellites.

ACKNOWLEDGMENT

The authors would like to thank the National Satellite Meteorology Center of China Meteorology Administration for

providing observation data and all geolocation information of FY-3C MWRI, colleagues from Shanghai Spaceflight Institute of TT&C and Telecommunication for MWRI antenna measurements and analysis in the prelaunch phase, and the Editor and Reviewers for their suggestions and valuable comments.

REFERENCES

[1] P. Zhang *et al.*, "Latest progress of the Chinese meteorological satellite program and core data processing technologies," *Adv. Atmos. Sci.,* vol. 36, pp. 1027–1045, 2019.
[2] R. Zhang, Z. Wang, and K. A. Hilburn, "Tropical cyclone rainfall estimates from FY-3B MWRI brightness temperatures using the WS algorithm," *Remote Sens.*, vol. 10, 2018, Art. no. 1770.
[3] J. Du *et al.*, "Inter-calibration of satellite passive microwave land observations from AMSR-E and AMSR2 using overlapping FY3B-MWRI sensor measurements," *Remote Sens.,* vol. 6, pp. 8594–8616, 2014.
[4] Y. Duan, Z. Wang, Y. Xiao, and W. Wang, "Simulating radiometric resolution of microwave humidity and temperature sounder onboard the FY-3D satellite," *IEEE Trans. Instrum. Meas.*, vol. 69, no. 9, pp. 6582–6594, Sep. 2020.
[5] G. Maschwitz, U. Lohnert, S. Crewell, T. Rose, and D. D. Turner, "Investigation of ground-based microwave radiometer calibration techniques at 530 hPa," *Atmos. Meas. Techn.,* vol. 6, pp. 2641–2658, 2013.
[6] H. Yang *et al.*, "The Fengyun-3 microwave radiation imager on-oribt verification," *IEEE Trans. Geosci. Remote Sens.,* vol. 49, no. 11, pp. 4552–4560, Nov. 2011.
[7] X. Xie, S. Wu, H. Xu, W. Yu, J. He, and S. Gu, "Ascending-descending bias correction of microwave radiation imager on board Fengyun-3C," *IEEE Trans. Geosci. Remote Sens.,* vol. 57, no. 6, pp. 3126–3134, Jun. 2019.
[8] H. Lawrence *et al.*, "An evaluation of FY-3C MWRI and assessment of the long-term quality of FY-3C MWHS-2 at ECMWF and the met office," Eur. Centre Medium-Range Weather Forecasts, Reading, U.K., ECMWF Tech. Memoranda 798, 2017.
[9] F. Carminati, N. Atkinson, and Q. Lu, "Preliminary assessment of FY-3D instruments towards their use in NWP systems," Met Office, London, U.K., Forecasting Res. Tech. Rep. 634, Jan. 2019.
[10] F. J. Wentz, "SSM/I version-7 calibration report," Remote Sens. Syst., Santa Rosa, CA, USA, Tech. Rep. 011012, 2013. [Online]. Available: http://images.remss.com/papers/rsstech/2012_011012_Wentz_Version-7_SSMI_Calibration.pdf
[11] S. Farrrar and L. Jones, "Estimation of TRMM microwave imager antenna temperature during deep space calibration maneuvers," in *Proc. Spec. Meeting Microw. Radiometry Remote Sens. Environ.*, Mar. 2014, pp. 215–220, doi: 10.1109/MicroRad.2014.6878943.
[12] S. Farrar, "An on-orbit calibration procedure for spaceborne microwave radiometers using special spacecraft attitude maneuvers," Ph.D. dissertation, Dept. Elect. Eng. Comput. Sci., Univ. Central Florida, Orlando, FL, USA, 2015.
[13] F. J. Wentz and D. Draper, "On-orbit absolute calibration of the global precipitation mission microwave imager," *J. Atmos. Ocean. Technol.,* vol. 33, no. 7, pp. 1393–1412, 2016.
[14] W. L. Jones, J. D. Park, S. Soisuvarn, L. Hong, P. W. Gaiser, and K. M. S. Germain, "Deep-space calibration of windsat radiometer," *IEEE Trans. Geosci. Remote Sens.*, vol. 44, no. 3, pp. 476–495, Mar. 2006.
[15] W. Berg *et al.*, "Intercalibration of the GPM radiometer constellation," *J. Atmos. Ocean. Technol.*, vol. 33, no. 12, pp. 2639–2654, Dec. 2016.
[16] S. Wu, X. Xie, M. Zhang, and H. Xu, "Development of FY-3/MWRI calibration on warm target and reflector emissivity," in *Proc. Global Space-Based Inter-Calibration Syst. Annu. Meeting*, 2018. [Online]. Available: http://gsics.atmos.umd.edu/pub/Development/20180319/9b_Shengli%20Wu_Development%20of%20FY-3MWRI%20Calibration%20on%20warm%20target%20and%20reflector%20emissivity.pptx
[17] F. Alquaied, R. Chen, and W. L. Jones, "Hot load temperature correction for TRMM microwave imager in the legacy brightness temperature," *IEEE J. Sel. Topics Appl. Earth Observ. Remote Sens.*, vol. 11, no. 6, pp. 1923–1931, Jun. 2018.
[18] D. B. Kunkee, S. D. Swadley, G. A. Poe, Y. Hong, and M. F. Werner, "Special sensor microwave imager sounder (SSMIS) radiometric calibration anomalies—Part I: Identification and characterization," *IEEE Trans. Geosci. Remote Sens.*, vol. 46, no. 4, pp. 1017–1033, Apr. 2008.
[19] R. A. Kroodsma, D. S. McKague, and C. S. Ruf, "Extension of vicarious cold calibration to 85–92 GHz for spaceborne microwave radiometers," *IEEE Trans. Geosci. Remote Sens.*, vol. 51, no. 9, pp. 4743–4751, Sep. 2013.
[20] M. C. Colton and G. A. Poe, "Intersensor calibration of DMSP SSM/I's: F-8 to F-14, 1987–1997," *IEEE Trans. Geosci. Remote Sens.*, vol. 37, no. 1, pp. 418–439, Jan. 1999.

Xinxin Xie received the B.S. degree in information engineering from Beihang University, Beijing, China, in 2006, and the PhD. degree in microwave remote sensing from the University of Cologne, Cologne, Germany, in 2012.

She is currently an Associate Professor with the School of Atmospheric Sciences, Sun Yat-Sen University, Zhuhai, China. From 2013 to 2016, she was with Meteorological Institute, University of Bonn, Bonn, Germany, where her research focused on quantitative precipitation estimates using polarimetric radar observations. From 2016 to 2020, she worked on satellite remote sensing with the Shanghai Spaceflight Institute of TT&C and Telecommunication. Her major research interests include clouds and precipitation with passive and active microwave remote sensing, and microwave radiometer calibration techniques.

Wanting Meng received the B.S. degree in spatial information and digital technology and the M.S. degree in software engineering from Shang Ocean University, Shanghai, China, in 2013 and 2016, respectively.

She is currently a Research Associate with the Shanghai Spaceflight Institute of TT&C and Telecommunication, Shanghai, China, in the field of microwave radiometer calibration techniques and GNSS-R remote sensing.

Kesong Dong received the master's degree in communication and information engineering from the Shanghai Institute of Aerospace Technology, Shanghai, China, in 2019.

He is currently with the Shanghai Spaceflight Institute of TT&C and Telecommunication, and mainly engaged in space-borne microwave radiometers calibration/validation and application, MWRI ground thermal/vacuum tests, and in-orbit recalibration.

Songyan Gu received the B.S. degree in atmospheric physics and the M.S. degree in radar meteorology from the Nanjing Institute of Meteorology, Nanjing, China, in 1985 and 1992, respectively, and the Ph.D. degree in atmospheric physics and environment from Peking University, Beijing, China, in 2003.

She is currently a Professor with National Satellite Meteorological Center, China Meteorological Administration, Beijing, China, in the field of the microwave instrument operational calibration and application.

Xue Li received the master's degree in electronic science and technology from the University of Electronic Science and Technology of China, Chengdu, China, in 2012.

She is with the Shanghai Spaceflight Institute of TT&C and Telecommunication, Shanghai, China. Her research interest focuses on microwave radiometer calibration techniques.